



**HAL**  
open science

## Thermo-mechanical behavior of Zircaloy-4 claddings under simulated post-DNB conditions

T. Jailin, Nicolas Tardif, J. Desquines, P. Chaudet, Michel Coret, M.-C.  
Baietto, V. Georgenthum

### ► To cite this version:

T. Jailin, Nicolas Tardif, J. Desquines, P. Chaudet, Michel Coret, et al.. Thermo-mechanical behavior of Zircaloy-4 claddings under simulated post-DNB conditions. *Journal of Nuclear Materials*, 2020, pp.151984. 10.1016/j.jnucmat.2020.151984 . hal-02437246v2

**HAL Id: hal-02437246**

**<https://hal.science/hal-02437246v2>**

Submitted on 15 Jan 2020 (v2), last revised 12 Jul 2022 (v3)

**HAL** is a multi-disciplinary open access archive for the deposit and dissemination of scientific research documents, whether they are published or not. The documents may come from teaching and research institutions in France or abroad, or from public or private research centers.

L'archive ouverte pluridisciplinaire **HAL**, est destinée au dépôt et à la diffusion de documents scientifiques de niveau recherche, publiés ou non, émanant des établissements d'enseignement et de recherche français ou étrangers, des laboratoires publics ou privés.



Distributed under a Creative Commons Attribution - NonCommercial - NoDerivatives 4.0  
International License

# Thermo-mechanical behavior of Zircaloy-4 claddings under simulated post-DNB conditions

T. Jailin<sup>a,b</sup>, N. Tardif<sup>b,\*</sup>, J. Desquines<sup>a</sup>, P. Chaudet<sup>b</sup>, M. Coret<sup>c</sup>, M.-C. Baidetto<sup>b</sup>, V. Georgenthum<sup>a</sup>

<sup>a</sup>Institut de Radioprotection et de Sûreté Nucléaire (IRSN), PSN-RES, Cadarache, Saint Paul lez Durance, France

<sup>b</sup>Univ Lyon, INSA-Lyon, CNRS UMR5259, LaMCoS, F-69621, France

<sup>c</sup>École Centrale de Nantes, GeM (UMR 6183), Nantes, France

## Abstract

The thermo-mechanical behavior of Zircaloy-4 claddings under simulated post-DNB RIA conditions was investigated. Around twenty experiments were performed in simulated post-DNB conditions, *i.e.* creep ballooning tests with heating rates greater than 1000°C/s. Two different levels of pressure of 7 and 11 bar were tested for temperatures of interest ranging from 840°C to 1020°C. A complex creep behavior was highlighted in this range of temperature. It appears very well correlated to the phase content present within the material during fast thermal transients. Tests with low thermal transients were also performed and evidence a strong impact of the heating rate on the thermo-mechanical properties of the claddings.

**Keywords:** Fast thermal transients, Full-field measurements, Creep, Zircaloy-4, RIA

## 1. Introduction

During the operating life of Pressurized Water Reactors (PWR) the nuclear reaction is controlled within the nuclear core using control rod made of neutron poison material. The Reactivity Initiated Accident (RIA) is one of the design basis accidents studied for PWR. It supposes an inadvertent insertion of reactivity in the nuclear power reactor. It may result from several possible scenarios, the most studied being the control rod ejection [1]. The RIA accident can be decomposed in two consecutive phases: the Pellet Clad Mechanical Interaction (PCMI) phase, followed by the post-Departure from Nucleate Boiling (post-DNB) phase. This second phase of the accident starts at the boiling crisis of the coolant, which leads to a brutal decreasing of the thermal transfer between the fuel claddings and the water. Subsequently, a high increase of the fuel claddings temperature occurs with thermal transients that can be greater than 1000°C/s up to temperatures exceeding 900°C [2]. In the same time, an internal pressure can appear within the claddings due to fission gas release. All these conditions may lead to the ballooning of the fuel rod until its potential burst. The aim of this work is to characterize the thermo-mechanical behavior of Zircaloy-4 fuel rods under such conditions.

Zircaloy-4 is widely used as fuel claddings material in PWR. It presents an allotropic phase transformation ( $\alpha \rightarrow \beta$ ) between 800°C to 1000°C upon heating at equilibrium. It switches from an hexagonal closed packed structure at low temperature, to a body centered cubic structure at high temperature [3]. A dual phase domain ( $\alpha + \beta$ ) is defined between the two single phase domains, where the two phases are present within the material.

It is well-known that the phase transition is highly dependant on the thermal history [4, 5, 6]. Moreover, the metallurgical state of the claddings has a strong impact on its thermo-mechanical properties [4, 7, 8]. Garde for instance [9], pointed out a superplastic behavior in the dual phase domain. Massih [10] proposed to model it by adding a grain boundary sliding contribution on the deformation, using a modified Ashby's model [11]. Some authors noticed a complex creep behavior in the dual phase domain that does not follow a classical power creep law, usually used to describe the creep behavior in Zirconium alloys [12, 13, 14].

A lot of experiments were performed in the last decades to investigate the thermo-mechanical behavior of fuel rods in the three domains  $\{\alpha, (\alpha + \beta), \beta\}$ . A special attention has been payed to accidental situations where the loading conditions can be very demanding. Due to the difficulty of reproducing well-controlled fast thermal transients, most of the experimental devices were developed to reproduce simulated LOCA (*Loss Of Coolant Accident*) conditions [13, 15, 16], or PCMI conditions [17, 18]. These experiments are characterized by isothermal tests or tests with low thermal transients. Extrapolating the data to post-DNB conditions is therefore somewhat adventurous... Chaieb *et al.* [19], investigated the plastic properties of Zircaloy-4 under thermal transients up to 560°C/s. They performed uniaxial and biaxial tensile tests with constant displacement rate, on claddings section and cruciform samples, respectively. They highlighted an impact of the heating rate on the mechanical properties for tests carried out with a constant strain rate of 0.5s<sup>-1</sup>.

Most of the experiments carried out to simulate post-DNB conditions were performed in experimental nuclear reactors [20, 21]. In this kind of tests the thermo-mechanical conditions cannot be well-controlled. Furthermore the many multi-physics

\*Corresponding author

Email address: [author@insa-lyon.fr](mailto:author@insa-lyon.fr) (N. Tardif)

couplings that take place within the nuclear core make the data analysis difficult. It follows that the creep behavior of the fuel rods remains poorly known after a fast thermal transient, especially in the dual phase domain where the metallurgical structure of the material may be far from the equilibrium state.

In this work, the experimental device ELLIE, developed by Campello and Tardif [22, 23], was updated to reproduce simulated thermo-mechanical post-DNB conditions on fuel cladding sections [24, 25]. Creep ballooning tests were performed with well-controlled thermal transients up to 1500°C/s using an induction heating system. Around twenty tests were carried out in simulated post-DNB conditions at two different levels of pressure for temperatures of interest ranging from 840°C to 1020°C. The use of full-field measurements methods enabled obtaining a large amount of data from each experiment by taking profit of the tests heterogeneities. These experiments highlighted a complex creep behavior in the domain of temperature investigated. It appears very well correlated to the phase content present within the material during fast thermal transients ( $\approx 1200^\circ\text{C/s}$ ). Tests with low thermal transients were also performed and showed a strong impact of the heating rate on the thermo-mechanical properties of the claddings.

The first section of this paper deals with the description of the test bench ELLIE. The second section presents two representative experiments performed in the  $\alpha$  and  $(\alpha + \beta)$  domains. The third section details the tests performed in "Simulated RIA" conditions and highlights a complex behavior in the dual phase domain. The fourth section presents the impact of the heating rate on the material creep behavior.

## 2. Experimental setup and procedure

### 2.1. Samples preparation

The specimens were cut from as-fabricated stress relieved annealed (SRA) Zircaloy-4 claddings (see the chemical composition in Table 1). The initial microstructure of the material is composed of thin and elongated grains and presents a texture having the [0002] direction at  $\pm 30^\circ$  from the radial direction of the tube [26]. The samples were 90mm long with an outer diameter of 9.5mm and a wall-thickness of 0.57mm. Their eccentricity was small and was estimated between 1 and 3% [22]. In order to perform stereo-correlation measurements the specimens were painted with a black undercoating and a white speckle pattern. Three thermocouples (type K, wires of 79 $\mu\text{m}$  diameter) were spot-welded on the sample outer surface in the region of interest (ROI) seen by the cameras (Figure 1.a).

Sn	Fe	O	Cr	C	Zr
1.29	0.21	0.13	0.11	0.016	bal.

Table 1: Stress relieved annealed Zircaloy-4 composition (in wt%).

### 2.2. The test bench ELLIE

The experimental device ELLIE was presented in detail in [23, 25]. Some reminders are given hereinafter. The test bench

is composed of a 10kN servo-hydraulic tensile machine. Figure 1 presents a picture and a scheme of a sample mounted on the device. The sample was connected onto the test machine using custom grips [27] reducing the distance between the jaws to 58mm. An internal pressure up to 70 bar can be imposed and controlled within the claddings during the whole tests using argon gas. A 30kW induction generator (ThermoInduzione TI3-30KW CT-110) was used to heat the samples with heating rates up to 1500°C/s. The induction generator frequency (92kHz) was chosen so that the thermal loading was uniform across the wall-thickness of the sample, even during fast thermal transients. The PID regulation was optimized to get low overshoots and the induction coil was designed to obtain the hottest point at the center of the ROI. The temperature regulation was achieved using a pyrometer (CTLM-2HCF4-C3, wavelength of 1.6 $\mu\text{m}$ ). All the experiments were performed within an enclosure where an argon flush was set up during the tests to prevent the samples from oxidation.

### 2.3. Tests processing

Two kinds of tests were performed to investigate the impact of the thermal transient on the material thermo-mechanical properties. Experiments, called "Simulated RIA", were performed with high heating rates to reproduce post-DNB conditions. The test procedure is depicted in Figure 2.a. In these experiments the mechanical loading was first applied. Once it was stabilized the sample was heated up in open loop with heating rate around 1200°C/s. The thermal regulation switched in closed loop when the temperature measured by the pyrometer reached a value 20°C lower than the target temperature (red circle in Figure 2.a).

Experiments with low heating rates, called "Simulated LOCA", were also carried out following the procedure used in [22]. The experimental procedure of these tests is presented in Figure 2.b. The thermal loading was first applied with a heating rate of 3°C/s. The mechanical loading was applied once the temperature was stabilized at the target value.

In all tests, a compressive force was applied simultaneously to the internal pressure to compensate the end caps effect. This force was calculated using the initial inner radius  $R_i$  of the claddings and the internal pressure  $P_i$  applied:

$$F_z = P_i \cdot \pi \cdot R_i^2. \quad (1)$$

For the two kinds of experiments the test time was set to zero once the thermal and mechanical loading were stabilized. This time offset is referred to  $t_0$  in Figure 2.

### 2.4. Optical means of measurement

Full-field optical techniques enable obtaining a large amount of data in one single experiment. The kinematic field can be obtained on the sample outer surface using digital images correlation (DIC) for instance. The thermal field can be either obtained using infrared (IR) thermography or near-infrared thermography (NIRT) techniques. The richness of these optical methods enables heterogeneous tests to be performed with complex loading conditions.

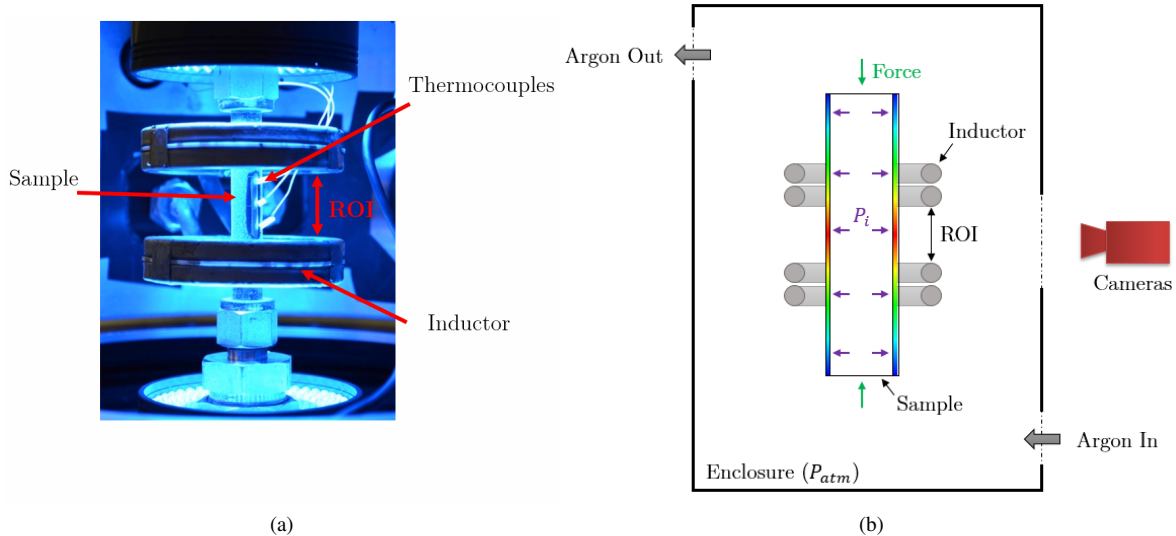


Figure 1: (a) Picture of the sample mounted on the device; (b) Scheme of the sample and the loading onto the device.

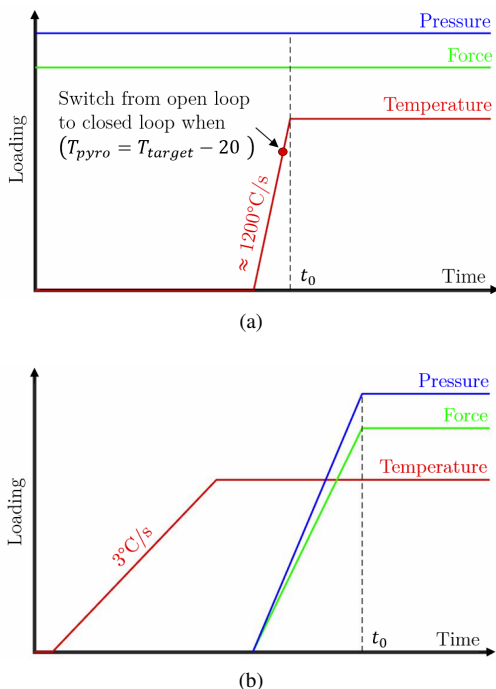


Figure 2: Scheme of loading for: (a) "Simulated RIA" experiments, (b) "Simulated LOCA" experiments.

Under very high thermal transients a tiny eccentricity between the specimen and the induction coil leads to a loss of axisymmetry of the thermal loading. Therefore it was chosen to force this eccentricity so that the hottest point on the sample was localized in front of the cameras. The non-axisymmetry of the thermal loading obtained induced heterogeneous creep strains. 3D optical full field measurements methods were used to record these loading heterogeneities.

A scheme of a top view of the experimental set-up is depicted in Figure 3. Two CMOS cameras 12MPx (VC-12MC-M65E0-

FM) recorded images of the ROI during the tests with a frequency up to 55Hz. The length of the ROI is characterized by the distance between the upper and the lower induction coils and was about 12mm. An example of an image of the ROI is given in Figure 4. The two cameras were equipped of 200mm macro optics (NIK AF MICRO-NIKKOR 200MM F/4 D IF-ED). Near infrared band-pass filters (wavelength  $\lambda = 865\text{nm} \pm 10\text{nm}$ ) were mounted on the optics. The pictures recorded by the cameras were used to compute both the kinematic field and the thermal field by stereo-correlation and NIRT methods, respectively. The two cameras were separated by an angle of  $18^\circ$  to perform a 3D surface reconstruction.

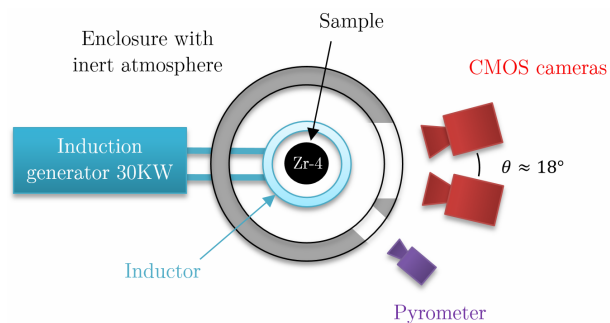


Figure 3: Scheme of a top view of the experimental set-up ELLIE.

### 2.5. Stereo-correlation (3D-DIC)

The 3D-surface displacements field was obtained using the global stereo-correlation software UFreckles developed by J. Réthoré [28], [29]. A finite elements basis of quadrilateral elements with linear shape functions was used to perform the images analysis with an element size of  $35 \times 35 \text{px}^2$  ( $1 \text{px} \approx 9 \mu\text{m}$ ). An example of a correlation mesh is given in Figure 4.b.

In order to avoid chromatic aberrations at high temperatures the calibration of the optical system was performed at low tem-

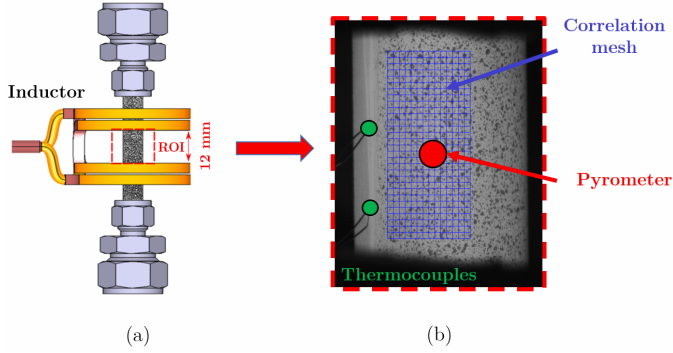


Figure 4: (a) Scheme of the sample mounted on the device; (b) Example of an image with the correlation mesh.

perature by lighting the sample in the near infrared domain using a LED ring at the wavelength  $\lambda = 860\text{nm}$ .

It is worth noting that because of the device geometry a "standard" calibration using calibration grids couldn't be performed. The calibration step was then achieved using the well-known geometry of the sample. The noise was finally estimated to be lower than  $1\mu\text{m}$  for the in-plane displacements and about  $5\mu\text{m}$  for the out-of-plane displacements.

### 2.6. Near InfraRed Thermography (NIRT)

The NIRT method was used to compute the thermal field at each time step. This method links the digital level intensity  $I$  of an image (*i.e.* the gray level of each pixel) to the temperature  $T$  using a radiometric model (Eq. 2) based on Planck's law:

$$T = \frac{K_1}{\ln\left(\frac{K_2}{I} + 1\right)}. \quad (2)$$

Two constants  $K_1$  and  $K_2$  have to be identified in this model [22].

Thermocouples are subjected to an inertia effect due to their intrusive nature, and the speckle pattern disturbs the optical thermal measurements. Therefore, an identification procedure that links the thermocouples, the pyrometer and the NIRT was developed to identify the radiometric model in a robust way. Furthermore, since the same images were used to compute both the thermal and the kinematics fields, a weak coupling between the two fields was developed. It follows that the thermal field was obtained at the exact same time and location that the kinematic field. No interpolation or smoothing operation were finally necessary on the thermal field. The accuracy on the temperature was estimated around 0.7% of the measured temperature [23]. More details on the procedure followed can be found in [30].

## 3. Results from two representative simulated RIA experiments

### 3.1. Phase fraction evolution

Before everything else the evolution of the  $\beta$  phase fraction with the temperature is given in Figure 5 for equilibrium condition and upon a heating rate of  $1200^\circ\text{C/s}$ . The equilibrium

data can be found in [4]. The  $1200^\circ\text{C/s}$  curve was obtained by a stress-free dilatometry experiment performed at an imposed heating rate of  $1200^\circ\text{C/s}$  on a GLEEBLE-3500 device [31]. The phase fraction accuracy is estimated to be 5% of the phase fraction between 10 and 90% of  $\beta$  content. Due to the nature of the dilatometry experiments the phase fraction cannot be well-trusted at the boundaries of the dual phase domain (*i.e.* between 0 and 10% of  $\beta$  and between 90 and 100% of  $\beta$ ). To avoid the inertia effect of the thermocouples the temperature was measured using a pyrometer leading to a thermal uncertainty of  $7^\circ\text{C}$ .

In the following the phase fraction obtained at equilibrium and upon a constant heating rate of  $1200^\circ\text{C/s}$  are referred to  $f_\beta^{eq}$  and  $f_\beta^{1200^\circ\text{C/s}}$ , respectively.

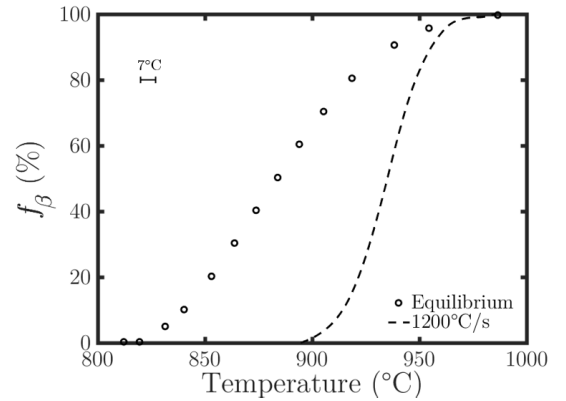


Figure 5:  $\beta$  phase fraction obtained on SRA-Zircaloy-4 samples at equilibrium conditions [4] and at a constant heating rate of  $1200^\circ\text{C/s}$  [31]

### 3.2. Experimental procedures of the two tests

Results from two tests that followed the experimental protocol presented in Figure 2.a are now used to describe a typical experiment analysis. The procedures of these two tests are depicted in Figure 6. One test, referred for convenience to the  $\alpha$ -test in the following, was carried out with a regulation temperature of  $850^\circ\text{C}$  and an internal pressure of 20 bar. The other test was run in the dual-phase domain ( $\alpha + \beta$ ) with a regulation temperature of  $940^\circ\text{C}$  and an internal pressure of 11 bar. The heating rates obtained for the  $\alpha$  and ( $\alpha + \beta$ ) experiments were  $1216^\circ\text{C/s}$  and  $1260^\circ\text{C/s}$ , respectively. Tiny overshoots (of  $+4^\circ\text{C}$  and  $+8^\circ\text{C}$ , respectively) can be observed. The times offsets of the two tests are represented by  $t_0$  in Figure 6. In both case the temperature stabilized at  $\pm 1^\circ\text{C}$  around the target value about 3.5s after  $t_0$ .

The heating rate is plotted during the transient for the two tests in Figure 7. Another test, carried out in the  $\beta$  domain, is also included in Figure 7, in order to see the evolution of the heating rate during the whole phase transition. A good repeatability of the thermal slope is obtained between the tests. A slight decrease of the heating rate is observed during each experiment between  $650$  and  $700^\circ\text{C}$ . It may be due to the intermetallic  $\text{Zr}(\text{Fe}, \text{Cr})_2$  dissolution. It can also be observed in the ( $\alpha + \beta$ ) and the  $\beta$  experiments that the heating rate decreases during the phase transition from around  $890^\circ\text{C}$ . It reaches a

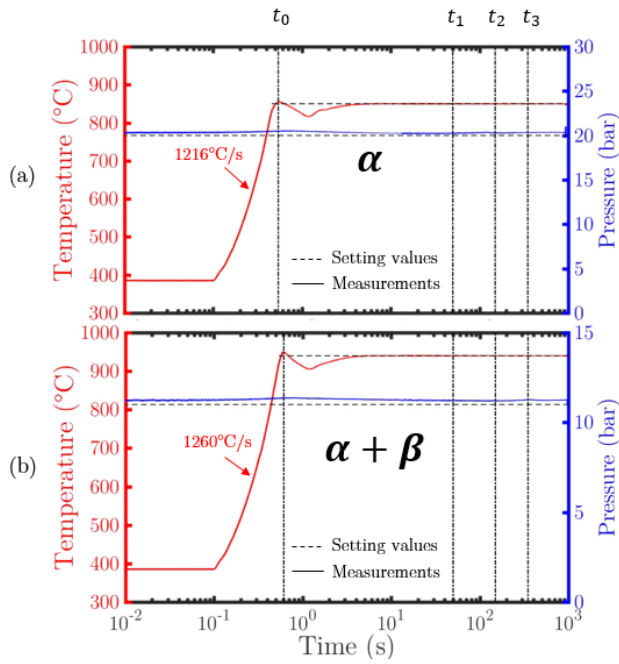


Figure 6: Experimental procedure of two tests with the setting values and the measurements obtained. (a) A test performed in the  $\alpha$  domain with a regulation temperature of 850°C and an internal pressure of 20 bar; (b) A test performed in the  $(\alpha + \beta)$  domain with a regulation temperature of 940°C and an internal pressure of 11 bar. Kinematic and thermal fields are presented in Figure 8 and 9 at times  $t_1$ ,  $t_2$ , and  $t_3$ .

minimal value of around 350°C/s at 940°C. These observations were well reproducible between all the tests performed.

Images were recorded at a frequency of 55Hz during the first fifteen seconds of the tests and then at a frequency of 1Hz until the end. Kinematic and associated thermal fields were computed on the outer surface of the specimen by 3D-DIC and NIRT, respectively, following the method described in section 2.

### 3.3. Analysis of the two tests

Figure 8 presents the kinematic field and the associated thermal field for three different test times  $\{t_1 = 50s; t_2 = 150s; t_3 = 350s\}$  for the  $\alpha$ -experiments. The kinematic fields given in Figure 8 correspond to the radial displacement fields normalized by the initial external radius of the sample. Thermal and kinematic fields are shown at the same test times of the  $(\alpha + \beta)$ -experiment in Figure 9. For both tests the hottest region was localized at the center of the ROI. The thermal heterogeneity in the ROI during the tests was about 20°C and 10°C for the  $\alpha$  and  $(\alpha + \beta)$ -experiments, respectively.

Two very different creep regimes were evidenced. In the  $\alpha$ -experiment the strain profile obtained may be seen as "standard", *i.e.* the more deformed area was localized at the hottest region. On the contrary, in the  $(\alpha + \beta)$ -experiment two more pronounced ballooning areas are visible, located at the upper and lower side of the ROI. These areas of larger strains were not localized at the hottest region like in the  $\alpha$ -test. Figure 10 presents the thermal and the kinematics data extracted from an

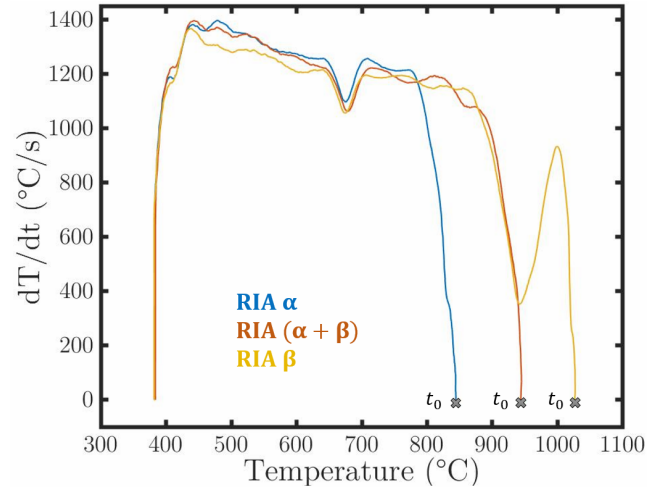


Figure 7: Evolution of the heating rate for the  $\alpha$  test, the  $(\alpha + \beta)$  test and a  $\beta$  test.

axial line referred to a red line in Figures 8 and 9. The area of maximal radial displacement is very well-correlated with the hottest region in the  $\alpha$ -experiment (Figure 10.a), while the opposite is observed in the  $(\alpha + \beta)$ -test (Figure 10.b).

Figure 11 shows for both tests the evolution of the radial displacement of all the nodes of the correlation meshes. The temperature of each point was computed by NIRT at each time step. Two main results can be highlighted. First, it can be observed in Figure 11.a that in the  $\alpha$ -experiment the points of maximal radial displacements correspond to the hottest one. Conversely, in the  $(\alpha + \beta)$ -experiment the Figure 11.b shows that the points of maximal radial displacement are the coolest one. These observations are in good agreement with the Figures 8, 9 and 10. It is shown in the following that this "non-standard" creep behavior occurring in the dual phase domain led at the end to the so-called "butternut shape" profile on the specimens. This profile is characterized by the presence of two ballooning areas on the samples while a single hottest region was localized at the center of the ROI.

Secondly, only a stationary creep is observed in the  $\alpha$ -experiment while a primary creep occurred in the  $(\alpha + \beta)$ -test. This primary creep is characterized by a decreasing of the strain rate during the first 150 seconds. The creep rate reached then a constant value, characteristic of the secondary stage of creep.

## 4. Experiments performed in "Simulated RIA" conditions

### 4.1. Tests performed

More than twenty tests were performed to study the thermo-mechanical behavior of Zircaloy-4 claddings in the dual phase domain under simulated post-DNB conditions. Heating rates around 1250°C/s were obtained in these tests. Two different levels of internal pressure, of 7 and 11 bar, were investigated. All the experiments followed the experimental procedure described in Figure 2.a.

As was underlined in section 3.2, the feedback control needs some time to stabilize the temperature, a classical thermal re-

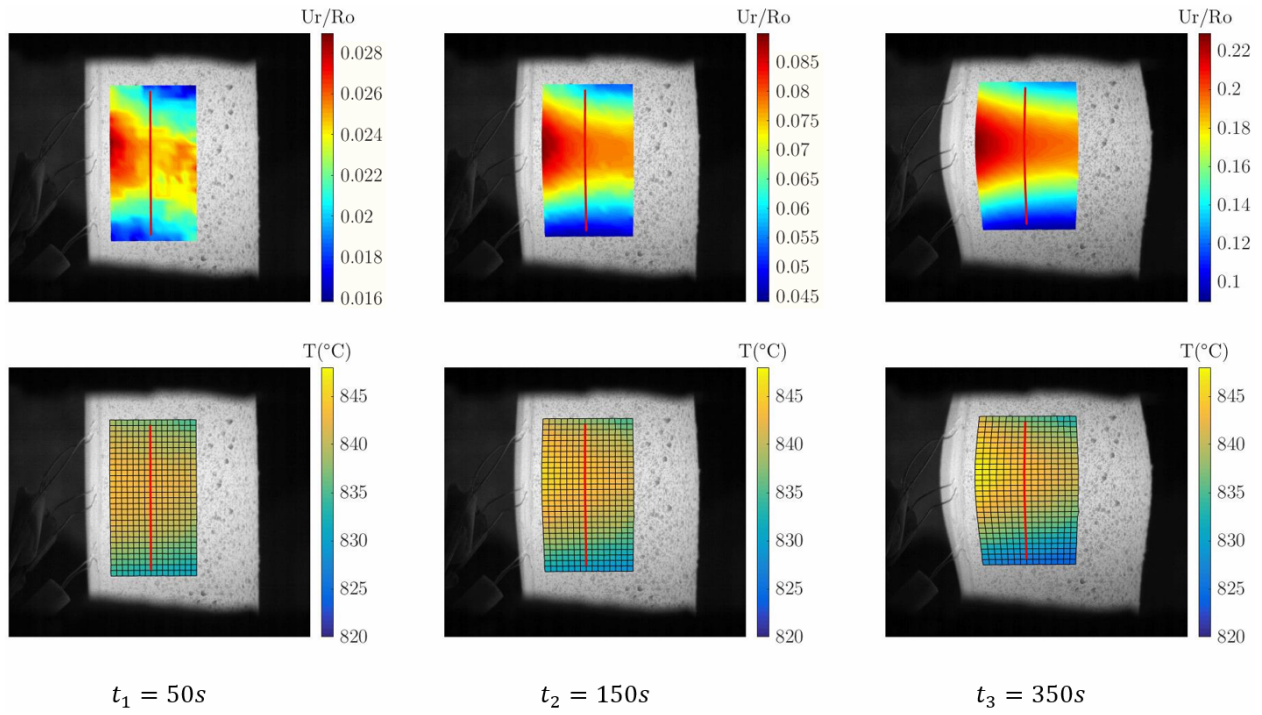


Figure 8: Kinematics and thermal field computed respectively by 3D-DIC and NIRT. These field were obtained at  $\{t_1 = 50s; t_2 = 150s; t_3 = 350s\}$  (see in Figure 6) for a test performed in the  $\alpha$  domain with a regulation temperature of  $850^{\circ}C$  and an internal pressure of 20 bar. Data extracted from the red axial line are presented in more details in the Figure 10.

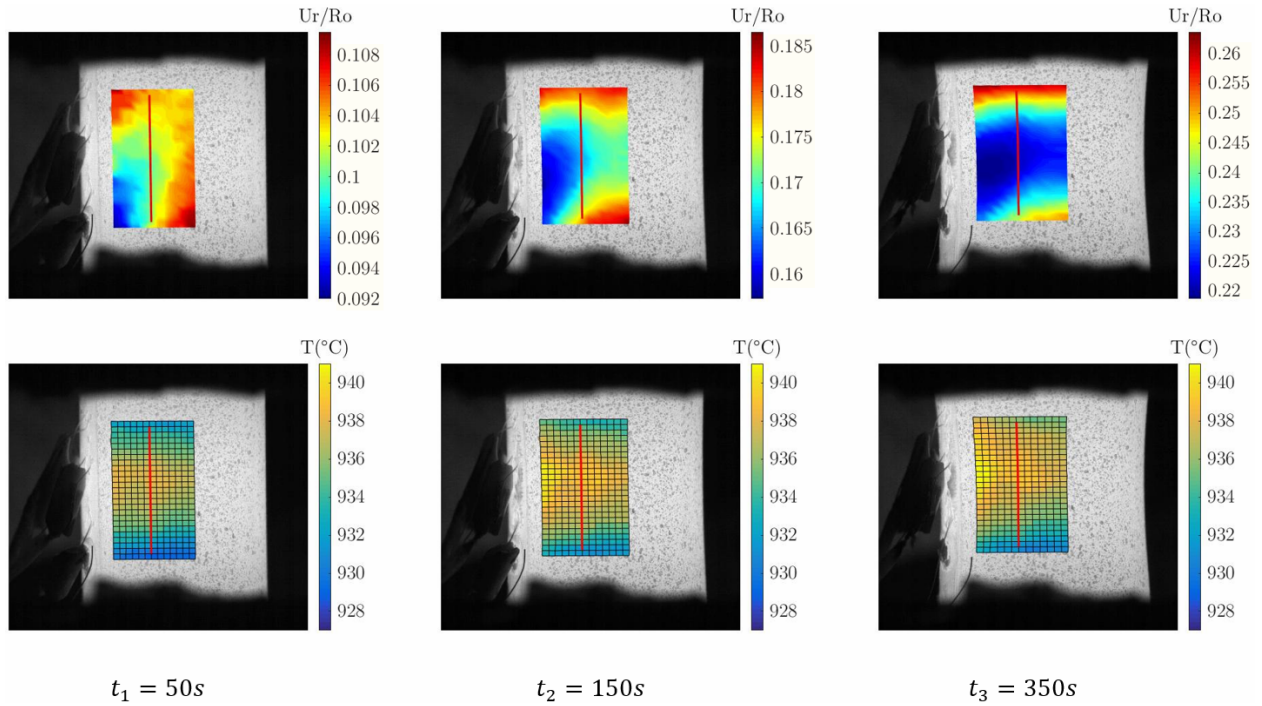


Figure 9: Kinematics and thermal field computed respectively by 3D-DIC and NIRT. These field were obtained at  $\{t_1 = 50s; t_2 = 150s; t_3 = 350s\}$  (see in Figure 6) for a test performed in the  $(\alpha + \beta)$  domain with a regulation temperature of  $940^{\circ}C$  and an internal pressure of 11 bar. Data extracted from the red axial line are presented in more details in the Figure 10.

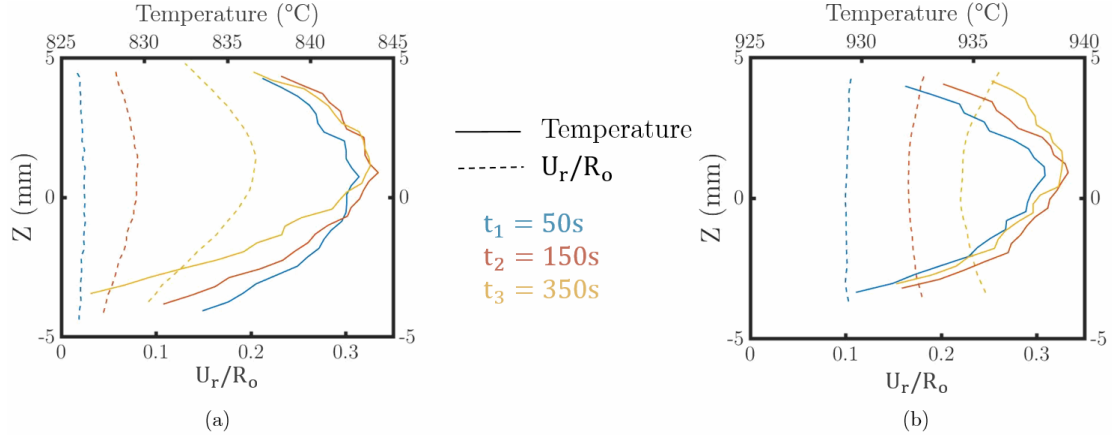


Figure 10: Thermal and kinematics data extracted from the red axial lines for (a) the  $\alpha$  experiment Figure 8, and (b) the  $(\alpha + \beta)$  experiment Figure 9.

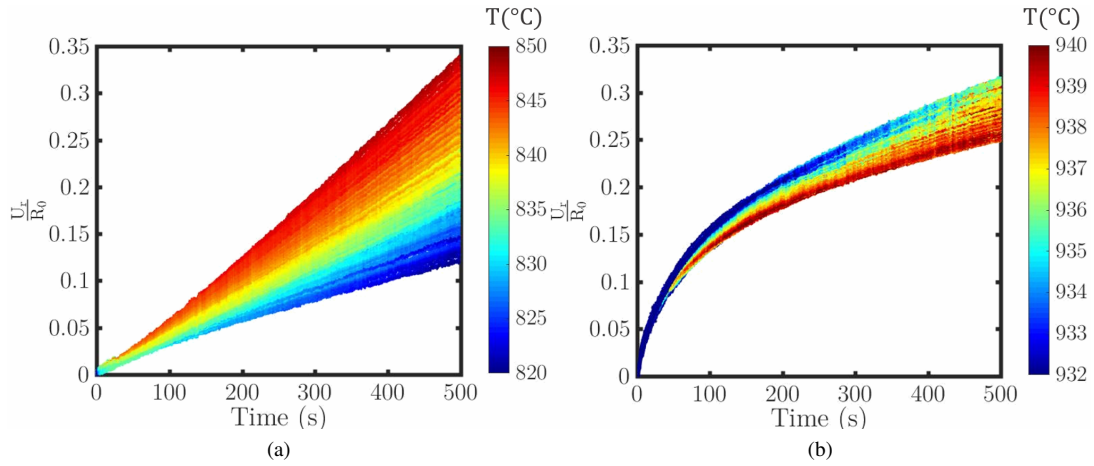


Figure 11: Radial displacements extracted from the stereo-correlation analysis for (a) the  $\alpha$  experiment, and (b) the  $(\alpha + \beta)$  experiment. The temperature of each point was computed by NIRT.

sponse recorded by the pyrometer is given in Figure 12. Two overshoot values,  $OS^+$  and  $OS^-$ , are here defined.  $OS^+$  is the difference between the maximal temperature reached at the end of the transient (at  $t_A$ ) and the regulation temperature.  $OS^-$  is the difference between the lowest value reached after  $t_A$  and the regulation temperature. In all tests  $OS^-$  is about  $-30^\circ\text{C}$  and the test time from which the temperature reaches  $\pm 1^\circ\text{C}$  around the regulation temperature is lower than 4 seconds ( $t_B - t_A$  in Figure 12).

The mean temperature obtained in the ROI, the mean thermal heterogeneity within the ROI at  $t = 10\text{s}$ , the heating rates obtained during the thermal transient, the  $OS^+$  overshoots and the internal pressure of the tests are given in Table 2.

In the following it is chosen to limit the study to the first ten seconds after the reference time  $t_0$  (Figure 2.a) of the experiments since it is the approximate maximum duration of the boiling crisis of a RIA.

#### 4.2. Experimental results

Figure 13 gathers the mean radial displacements rates normalized by the initial radius obtained during the first ten sec-

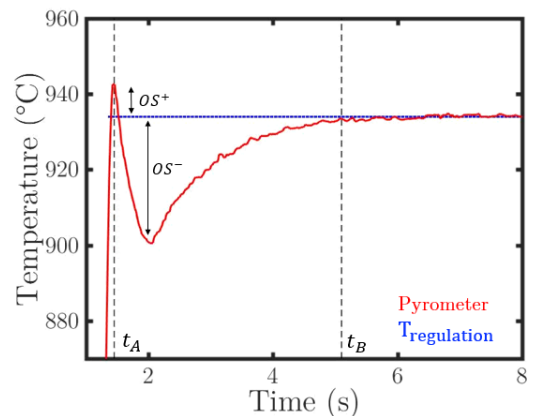


Figure 12: Pyrometer response and regulation temperature obtained for the test referred as RIA 7 in table 2.  $OS^+$  is the difference between the maximal temperature reached at the end of the transient (at  $t_A$ ) and the regulation temperature.  $OS^-$  is the difference between the lower value reached after  $t_A$  and the regulation temperature.  $t_B$  is defined as the time from which the temperature reaches  $\pm 1^\circ\text{C}$  around the regulation temperature.



$P_i = 7 \text{ bar}$					$P_i = 11 \text{ bar}$				
Exp. no	$T_{ROI}$ (°C)	$dT/dt$ (°C/s)	$OS^+$ (°C)	$\Delta T$ (°C)	Exp. no	$T_{ROI}$ (°C)	$dT/dt$ (°C/s)	$OS^+$ (°C)	$\Delta T$ (°C)
RIA 17	853	1285	24	841 - 863	RIA 08	854	1210	22	844 - 865
RIA 31	870	1271	7	864 - 878	RIA 30	868	1291	20	861 - 877
RIA 16	890	1240	17	883 - 899	RIA 9	880	1247	16	872 - 893
RIA 28	909	1235	1	902 - 917	RIA 21	883	1334	18	870 - 891
RIA 23	925	1280	12	914 - 937	RIA 29	906	1310	4	895 - 915
RIA 15	954	1216	0	942 - 967	RIA 11	928	1232	2	918 - 935
RIA 25	968	1264	4	963 - 975	RIA 7	933	1218	9	923 - 938
RIA 22	977	1295	0	965 - 994	RIA 14	953	1245	0	945 - 964
RIA 24	999	1263	29	994 - 1009	RIA 18	957	1226	0	945 - 970
RIA 26	1009	1222	0	1002 - 1019	RIA 19	972	1247	5	960 - 987
					RIA 20	973	1231	15	971 - 998
					RIA 10	980	1275	0	968 - 983
					RIA 12	1001	1223	1	993 - 1004
					RIA 27	1015	1310	7	991 - 1035

Table 2: Experimental conditions of the "Simulated RIA" experiments performed.  $T_{ROI}$  represents the temperature computed at the center of the ROI by NIRT.  $dT/dt$  is the mean value of the thermal transient measured by the pyrometer.  $OS^+$  is the difference between the maximal temperature reaches at the end of the transient (at  $t_0$ ) and the regulation temperature (Figure 12).  $\Delta T$  gives the mean thermal distribution within the ROI at  $t = 10s$ .

onds of the tests. These points were computed by linearizing the radial displacement evolution of each node of the correlation meshes of all tests. The associated temperatures are the mean value of each node and were computed by NIRT. The evolution of the  $\beta$  phase fraction with the temperature is also plotted in Figure 13 for the equilibrium condition and for a heating rate of  $1200^\circ\text{C/s}$ .

The authors point out that these mean displacement rates values were computed whereas the stationary creep stage was not reached yet. General tendencies can nevertheless be extracted.

As expected the tests performed with an internal pressure of 11 bar led to higher creep rates than the one performed with an internal pressure of 7 bar. A similar trend of the creep rate evolution with the temperature is observed between the two levels of pressure.

Three different domains of creep behavior can be identified in Figure 13. The first one is defined below  $\simeq 910^\circ\text{C}$ , *i.e.* in the  $\alpha$  and  $(\alpha, \alpha + \beta)$  domains, where  $f_\beta^{1200^\circ\text{C/s}} \leq 10\%$ . In this first domain the creep rate increases with the temperature. It follows that only one central ballooning area was observed on the samples, like in the  $\alpha$ -experiment detailed in the previous section. Label 1 in Figure 14 shows the post-mortem shape of a sample loaded at  $870^\circ\text{C}$ . Only one balloon is present at the location of the hot spot induced by the induction heating device. The sample referred to label 2 in Figure 14 was issued from an experiment performed in the upper temperature range of this first creep domain ( $906^\circ\text{C}$ ). A single large deformed region was obtained on the specimens. This large deformed region is characteristic of the transition in the creep behavior between the first and the second domain identified. In this temperature range (around  $910^\circ\text{C}$ ), the creep rate does not strongly depend on the temperature.

The second domain is defined from  $910^\circ\text{C}$  to  $970^\circ\text{C}$ , *i.e.* between  $f_\beta^{1200^\circ\text{C/s}} \simeq 10\%$  and  $f_\beta^{1200^\circ\text{C/s}} \simeq 100\%$ . In this second

domain the creep rate evolution reverses and decreases while the temperature increases. For the experiments performed in this domain two well-defined ballooning areas were obtained on the samples. This double balloons profile led to the so-called "butternut shape" on the specimens, already mentioned for the  $(\alpha + \beta)$ -experiment in section 3. The so-called "butternut shape" is observed on the sample referred to label 3 in Figure 14. This specimen was issued from an experiment carried out with a regulation temperature of  $954^\circ\text{C}$  and with an internal pressure of 7 bar. The authors recall that in all tests a single hot spot was localized at the center of the samples as presented in Figure 10.b. The temperature is then decreasing toward the jaws as illustrated in Figure 14.

The third domain is defined above  $970^\circ\text{C}$ . It begins at the  $(\alpha + \beta) \rightarrow \beta$  transition. Above this transition the creep rate increases strongly with the temperature. Three ballooning areas were obtained on the specimens experiments performed in this domain, as shown for instance in the sample labelled 4 in Figure 14. One localized at the center of the sample where the temperature was maximal and two from either side of the ROI. The presence of these two eccentric ballooned areas can be explained by the second domain of creep defined between  $910^\circ\text{C}$  to  $970^\circ\text{C}$  where the creep rates are higher at low temperatures.

Figure 13 gathers the creep rates measured during this study. It can be observed that in the two phase region the creep rate decreases with increasing temperature. Conversely, it increases with temperature in the  $\alpha$  and  $\beta$  domains. This two phase creep regime induces the double ballooning profile, as observed in Figure 14.

#### 4.3. Metallurgical analysis

Following the tests, metallurgical analysis were performed on the samples using an optical microscope. Axial and radial sections were cut from the specimens in the region facing the

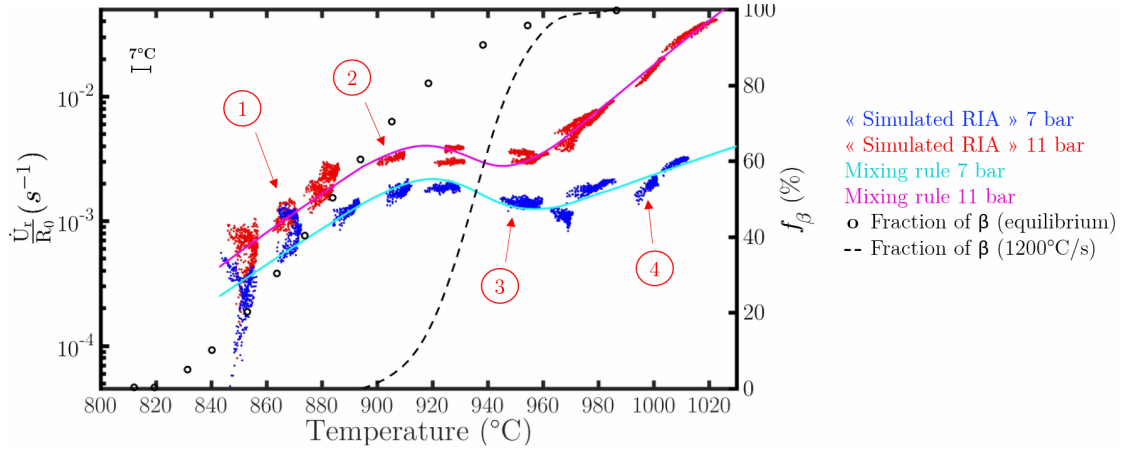


Figure 13: Mean radial displacement rates normalized by the initial radius obtained during the first 10 seconds of the tests. The fraction of  $\beta$  was obtained by a stress-free dilatometry experiment carried out with a constant heating rate of  $1200^{\circ}\text{C/s}$ . Samples issued of tests labelled 1 to 4 are presented Figure 14.

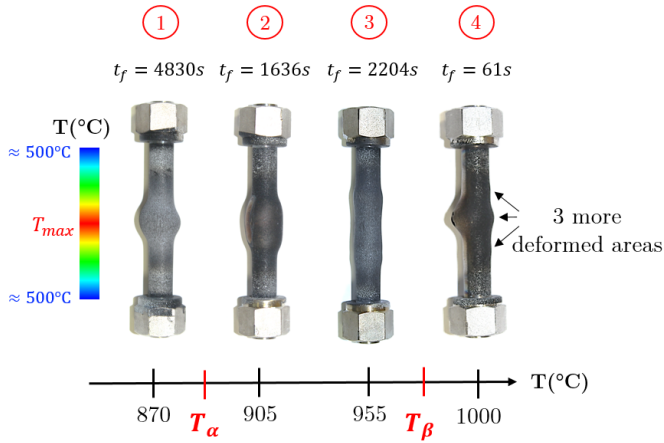


Figure 14: Example of 4 samples that have been tested. For each case the temperature was maximal at the center of the sample and was decreasing towards the jaws.  $t_f$  is the final test time of the experiments.

cameras and in the more deformed areas. No quantitative estimation of the phase fraction was possible in the dual phase domain but the  $(\alpha + \beta) \rightarrow \beta$  can be clearly distinguished. A cooling rate of around  $-50^{\circ}\text{C/s}$  was obtained at the center of the ROI by cutting power.

Figure 15 shows four micrographs obtained after an axial cut performed at the center of the RIA 25 sample. This test lasted 135 seconds with a regulation temperature of  $968^{\circ}\text{C}$  and an internal pressure of 7 bar. The maximal temperatures associated to the micrographs were computed by NIRT. The maximal temperature of the micrograph (a) is not known accurately because it was outside the ROI. The maximal temperature was then estimated knowing that the temperature at the jaws is around  $500^{\circ}\text{C}$ .

A strong evolution in the metallurgical structure depending on the maximal temperature reached is observed. A fully recrystallized microstructure, with small and equiaxed grains, is visible in Figure 15.a. In this area the temperature was lower than the  $(\alpha + \beta) \rightarrow \beta$  transition. In Figure 15.b the grains are slightly bigger and few oxygen enriched set of parallel thin nee-

dles are observed. Large grains, containing coarse needles, are observed in Figure 15.c and in Figure 15.d, where the maximal temperatures were  $969^{\circ}\text{C}$  and  $976^{\circ}\text{C}$ , respectively. This is characteristic of a fully ex- $\beta$  structure.

In all the samples, the areas that exceeded  $970^{\circ}\text{C}$  present a microstructure with large ex- $\beta$  grains containing needle shaped precipitates comparable to the one illustrated in Figures 15.c.d. Structures with small and equiaxed grains were obtained when the temperature was lower than  $970^{\circ}\text{C}$ . These observations are consistent with the  $(\alpha + \beta) \rightarrow \beta$  transition obtained in the dilatometry experiments (Figure 5).

#### 4.4. Discussion

In this work creep ballooning tests were performed between  $840^{\circ}\text{C}$  and  $1020^{\circ}\text{C}$ . Figure 13 gathers the mean radial displacements rate of the tests, assuming secondary creep regime, during the first ten seconds. The thermo-mechanical behavior observed in the temperature range investigated seems to be very well related to the phase fraction present within the material obtained at  $1200^{\circ}\text{C/s}$ . This complex behavior is characterized in the dual phase domain by a decreasing of the strain rate as the temperature increases. Similar observations has already been seen by some authors in the literature.

Frechinet [12] and Kaddour [13] noticed a decreasing of the strain rate in the  $(\alpha + \beta)$  domain with increasing temperature, for tensile tests performed on Zircaloy-4 and Zr-1%NbO tubular samples. For tests performed on sheet samples in M5 alloy, Trego [14] observed a comparable behavior, but only in the upper range of the  $(\alpha + \beta)$  domain. He also highlighted a steep transition in the creep behavior and in the grains size at the pure  $\beta$  domain transition. He explained this transition by the vanishing of the remaining  $\alpha$  phase that was present at the  $\beta$  grains boundaries. This remaining  $\alpha$  phase would prevent the  $\beta$  grains growth. Its complete transformation into  $\beta$  phase would then release the  $\beta$  grains growth and thus lead to the third domain of creep behavior identified in Figure 13. Though the testing conditions are different from this work these conclusions are in good agreements with (i) the  $\beta$  phase evolution obtained by the dilatometry experiment, (ii) the strong transition in the creep

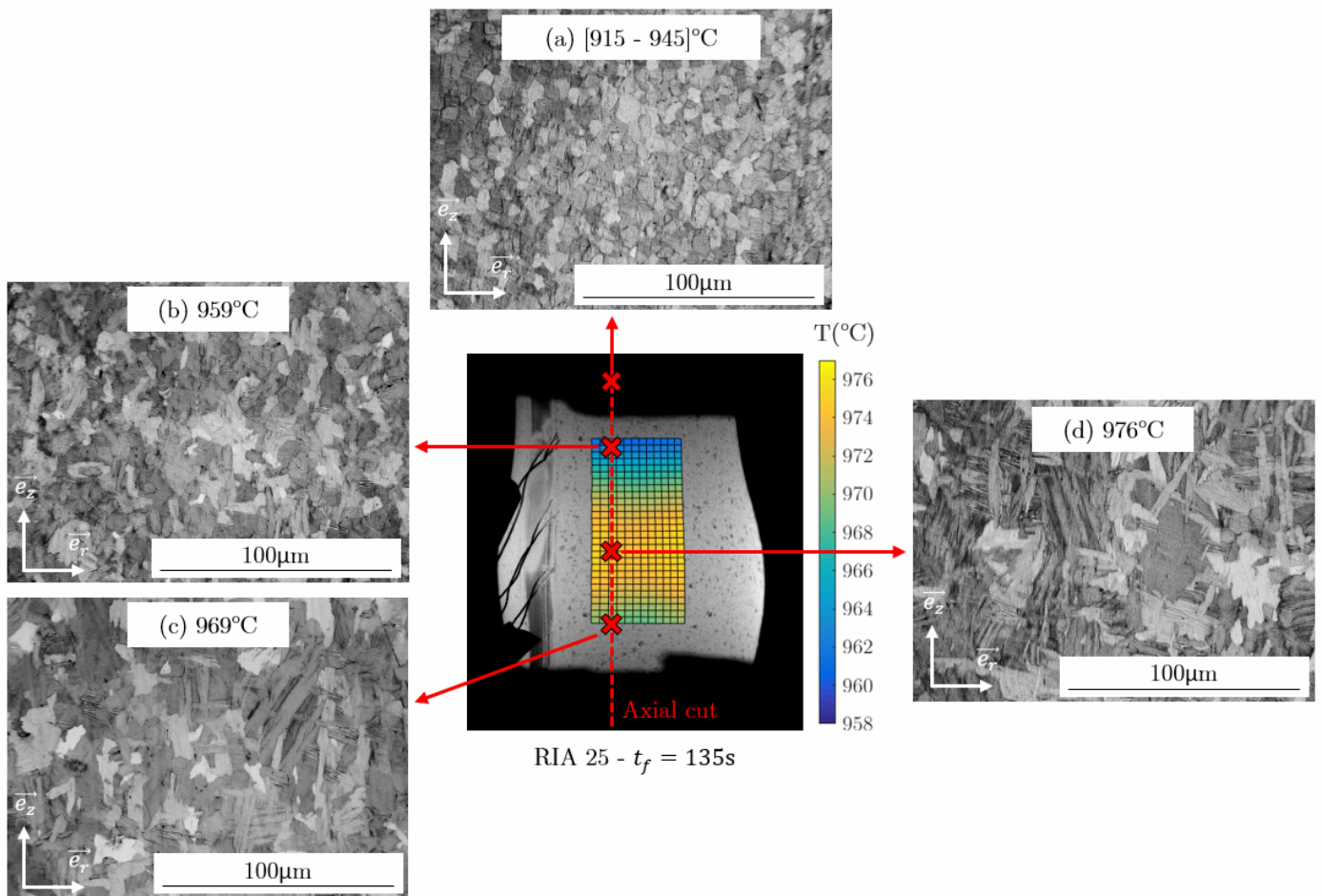


Figure 15: Metallurgical analysis obtained from an axial cut of the RIA 25 sample along the red dashed line. The test lasted 135 seconds. Four micrographs are shown with their corresponding maximal temperature reached. The central image shows the thermal field computed by NIRT at the end of the test.

behavior observed around 970°C, and (iii) the metallurgical observations performed on the samples post-mortem.

Structural effects may take place within the samples during the tests due to the thermal heterogeneity on the specimens. Finite element simulations and metallurgical studies will be carried out to identify more accurately the deformation mechanisms of the material.

The decrease of the creep rate in the second domain may result from a serial distribution of the two phases within the material. Assuming this, it follows:

$$\Sigma = \sigma_\alpha = \sigma_\beta \quad (3)$$

$$\dot{E} = \dot{\epsilon}_\alpha \cdot (1 - f_\beta) + \dot{\epsilon}_\beta \cdot f_\beta \quad (4)$$

Where  $\Sigma$ ,  $\sigma_\alpha$  and  $\sigma_\beta$  are the homogenized stress, the stress in the  $\alpha$  phase and the stress in the  $\beta$  phase, respectively.  $f_\beta$  is the  $\beta$  phase fraction. And  $\dot{E}$ ,  $\dot{\epsilon}_\alpha$  and  $\dot{\epsilon}_\beta$  are the homogenized strain rate, the strain rate in the  $\alpha$  phase and the strain rate in the  $\beta$  phase, respectively. The strain rates can be substituted by the displacement rate so that:

$$\dot{U}_r = \dot{U}_r^\alpha \cdot (1 - f_\beta) + \dot{U}_r^\beta \cdot f_\beta \quad (5)$$

Where  $\dot{U}_r$ ,  $\dot{U}_r^\alpha$  and  $\dot{U}_r^\beta$  are the homogenized radial displacement rate, the radial displacement rate in the  $\alpha$  phase and the radial displacement rate in the  $\beta$  phase, respectively.

Assuming that the creep behavior of individual phases follow a thermally activated Norton's creep law it can be written that under constant applied stress:

$$\dot{U}_r^i = A_i \cdot \exp\left(\frac{B_i}{T}\right) \quad \text{with } i = \{\alpha; \beta\} \quad (6)$$

Where  $T$  is the temperature and  $\{A_i; B_i\}$  represent four constants associated to the pure monophasic domains  $\alpha$  and  $\beta$ .

Assuming small strains and using the Equations 5 and 6 with the phase fraction evolution  $f_\beta^{1200^\circ\text{C/s}}$  obtained by dilatometry at 1200°C/s it becomes possible to obtain an homogenized evolution of the radial displacement rate from 840°C to 1020°C. Figure 13 depicts the results for the experiments performed at 7 and 11 bar. This simple homogenized behavior, based on a linear mixing rule on the strains [32], enables reproducing quite well the experimental data obtained in the dual phase domain. The authors point out that the assumptions postulated will have to be supported by finite elements simulations. These calculations will enable to account for structural effects inherent of ballooning tests.

## 5. Impact of the thermal transient

### 5.1. Tests performed in "Simulated LOCA" conditions

Some experiments were performed in "simulated LOCA" conditions to investigate the impact of the thermal transient on the material creep properties. The experimental procedure of these tests is described in Figure 2.b and the nominal loading conditions applied are given in Table 3.

Exp. no	$T_{ROI}$ (°C)	$P_i$ (bar)	$\Delta T$ (°C)
LOCA 10	863	11	848 - 870
LOCA 08	901	11	884 - 905
LOCA 04	931	7	922 - 934
LOCA 06	973	7	965 - 976
LOCA 11	987	11	969 - 999
LOCA 09	989	7	968 - 998
LOCA 13	1010	7	1003 - 1015

Table 3: Experimental conditions of the "Simulated LOCA" experiments performed.  $T_{ROI}$  is the temperature computed at the center of the ROI by NIRT.

### 5.2. Comparison between the two testing conditions

The mean radial displacements rates obtained during the first ten seconds of the "Simulated LOCA" tests are presented in Figure 16. It can be observed that the creep rates obtained subsequently to a slow heating transient are significantly smaller than the one obtained in "simulated RIA" conditions. For the same nominal loading conditions of temperature and pressure differences in the creep rates exceeding a decade are obtained depending on the thermal transient.

Butternut shape profiles were also obtained for the experiments carried out in the dual phase domain in "Simulated LOCA" conditions. The decreasing of the creep rate while the temperature increases appears clearly in Figure 16 for the tests referred to "LOCA 04", "LOCA 06" and "LOCA 09" in Table 3. Furthermore, similarly to the experiments performed in "Simulated RIA" conditions, a high increase of the strain rate is also observed between the tests "LOCA 09" and "LOCA 13", located at the  $(\alpha + \beta) \rightarrow \beta$  transition.

These results showed a strong impact of the thermal history on the material mechanical properties. The allotropic phase transformation is a non-instantaneous phenomenon highly dependant on the heating rate. Moreover, other metallurgical phenomena like grains growth, variants selection, transformation induced plasticity or dynamic recrystallisation for instance, are time dependant and linked to the crystallographic structure of the material. Two samples initially identical may be in a completely different metallurgical state at high temperature depending on their thermal history. Further investigations should be conducted in order to better identify the mechanisms responsible of the differences observed between "Simulated LOCA" and "Simulated RIA" experiments.

## 6. Summary and conclusions

A creep ballooning device was set-up to reproduce simulated RIA post-DNB conditions on fuel rods sections. More than twenty ballooning tests were performed at regulation temperatures ranging from 840°C to 1020°C with heating rates around 1200°C/s. Two different levels of pressure of 7 and 11 bar were investigated. The use of full-field optical methods enabled heterogeneous tests to be performed from which a large amount of data could be recorded and further processed.

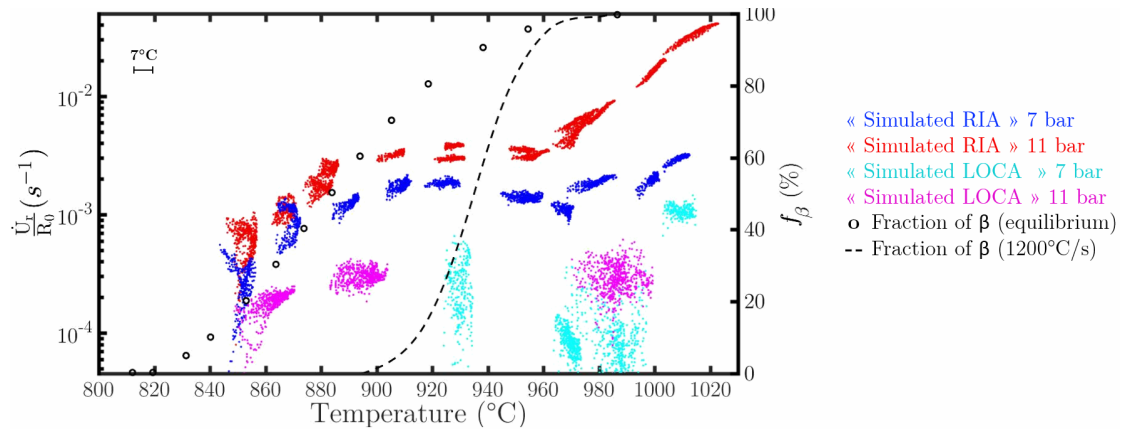


Figure 16: Mean radial displacement rates normalized by the initial radius obtained during the first 10 seconds of the tests. The fraction of  $\beta$  was obtained by a stress-free dilatometry experiment carried out with a constant heating rate of 1200°C/s.

These tests evidenced three domains of behavior that appear to be very-well correlated with the phase fraction present within the material obtained at such heating rates:

- The first domain is defined from 840°C to 910°C ( $f_\beta^{1200^\circ\text{C/s}} \leq 10\%$ ). In this temperature range the behavior may be seen as "standard" with a creep rate increasing with the temperature.
- From 910°C ( $f_\beta^{1200^\circ\text{C/s}} \simeq 10\%$ ) to 970°C ( $f_\beta^{1200^\circ\text{C/s}} \simeq 100\%$ ) the trend reverses and the creep rate decreases while the temperature increases. The experiments performed in this domain led to the so-called "butternut shape" profile on the samples.
- Above 970°C, *i.e.* at the pure  $\beta$  domain transition, the creep behavior changes steeply and the creep rate increases anew with the temperature. In this domain the grains size observed post-mortem is much more important and contained needle shaped precipitates, characteristic of a fully ex- $\beta$  structure.

Such a behavior was already exhibited by Trego on M5 material in simulated LOCA conditions. He postulated that the changes in the creep mechanism observed at the  $(\alpha + \beta) \rightarrow \beta$  transition can be explained by the vanishing of the remaining  $\alpha$  phase that was located at the  $\beta$  grains boundaries. Small  $\alpha$  grains are expected to behave like precipitates, anchoring  $\beta$  grain boundaries and behaving as well as obstacles for dislocation motion. The complete vanishing of the  $\alpha$  grains would released the  $\beta$  grains growth that was before inhibited and thereby lead to a high increasing of the creep rate.

A simple homogenization law, based on the assumption that the two phases are in a serial distribution, has been proposed to model the creep behavior in the  $(\alpha + \beta)$  domain. Using the phase fraction, obtained by a stress-free dilatometry experiment performed at very high heating rate, combined with a linear mixing rule, an homogenized behavior could be obtained from 840°C to 1020°C. It enables reproducing quite well the creep rate evolution in all the temperature range addressed in

the study. Further analysis using finite element simulations will be conducted in order to take into account the potential structural effects occurring within the samples. Thanks to the full-field measurements a constitutive creep law could be identified accurately by a finite element method updating (FEMU) algorithm.

Experiments were also performed with slow heating rates to investigate the impact of the thermal history on the creep material properties. The results showed significantly higher creep rates for the experiments carried out with a high heating rate. Two initially identical samples may be in a completely different metallurgical state at high temperature since metallurgical phenomena - phase transition, grains growth...- are time dependant. Additional metallurgical studies should be performed to identify and model the mechanisms responsible of the differences observed.

## Data availability

The raw and processed data of the current study are available from the corresponding author on request.

## Acknowledgments

The authors acknowledge with thanks financial support of this work from EdF and Institut Carnot Ingénierie@Lyon. The authors want also to express their thanks to J. Réthoré for allowing access to the UFreckles software and ATYS Consulting Group for helping on the induction problematic.

## References

- [1] P. Rudling, L. O. Jernkvist, F. Garzarolli, R. Adamson, T. Mahmood, A. Strasser, C. Patterson, Nuclear Fuel Behaviour under RIA Conditions, Tech. Rep. December, ANT International (2016).
- [2] V. Bessiron, Modelling of clad-to-coolant heat transfer for RIA applications, *Journal of Nuclear Science and Technology* 44 (2) (2007) 211–221. doi:10.1080/18811248.2007.9711275.
- [3] S. Banerjee, P. Mukhopadhyay, Phase Transformations: Examples from Titanium and Zirconium Alloys, Elsevier, 2010.

- [4] T. Forgeron, J. C. Brachet, F. Barcelo, A. Castaing, J. Hivroz, J. P. Mardon, C. Bernaudat, Experiment and Modeling of Advanced Fuel Rod Cladding Behavior Under LOCA Conditions: Alpha-Beta Phase Transformation Kinetics and EDGAR Methodology, in: *Zirconium in the Nuclear Industry: Twelfth International Symposium*, 2000, pp. 256–278. doi:10.1520/STP14303S.
- [5] R. A. Holt, The beta to alpha phase transformation in Zircaloy-4, *Journal of Nuclear Materials* 35 (1970) 322–334. doi:10.1016/0022-3115(70)90216-3.
- [6] E. J. Mittemeijer, Analysis of the kinetics of phase transformations, *Journal of Materials Science* 27 (15) (1992) 3977–3987. doi:10.1007/BF01105093.
- [7] J. J. Kearns, J. E. Mccauley, F. A. Nichols, Effect of alpha/beta phase constitution on superplasticity and strength of Zircaloy-4, *Journal of Nuclear Materials* 61 (2) (1976) 169–184. doi:10.1016/0022-3115(76)90081-7.
- [8] H.-J. Sell, E. Ortlieb, Effects of alpha-beta transformation on high temperature (LOCA) creep behavior of Zr-alloys., in: *Zirconium in the Nuclear Industry: Thirteenth International Symposium*, 2002, pp. 658–672. doi:10.1520/STP11410S.
- [9] A. M. Garde, H. M. Chung, T. F. Kassner, Micrograin superplasticity in Zircaloy at 850°C, *Acta Metallurgica* 26 (1) (1978) 153–166. doi:10.1016/0001-6160(78)90212-2.
- [10] A. R. Massih, High-temperature creep and superplasticity in zirconium alloys, *Journal of Nuclear Science and Technology* 50 (1) (2013) 21–34. doi:10.1080/00223131.2013.750054.
- [11] M. F. Ashby, R. A. Verrall, Diffusion-accommodated flow and superplasticity, *Acta Metallurgica* 21 (2) (1973) 149–163. doi:10.1016/0001-6160(73)90057-6.
- [12] S. Fréchet, Transformations et comportement du Zircaloy-4 en conditions anisothermes, Ph.D. thesis, Ecole Nationale Supérieure des Mines de Paris (2001).
- [13] D. Kaddour, S. Frechinet, A. F. Gourgues, J. C. Brachet, L. Portier, A. Pineau, Experimental determination of creep properties of zirconium alloys together with phase transformation, *Scripta Materialia* 51 (6) (2004) 515–519. doi:10.1016/j.scriptamat.2004.05.046.
- [14] G. Trégo, Comportement en fluage à haute température dans le domaine biphasé ( $\alpha + \beta$ ) de l’alliage M5., Ph.D. thesis, Ecole Nationale Supérieure des Mines de Paris (2011).
- [15] M. Réocreux, E. F. Scott de Martinville, A study of fuel behavior in PWR design basis accident: an analysis of results from the PHEBUS and EDGAR experiments, *Nuclear Engineering and Design* 124 (3) (1990) 363–378. doi:10.1016/0029-5493(90)90301-D.
- [16] C. Dominguez, Effect of pre-oxide and hydrogen on creep of Zircaloy-4 at 1123K, *Journal of Nuclear Materials* 511 (2018) 446–458. doi:10.1016/j.jnucmat.2018.09.047.
- [17] B. Cazalis, J. Desquines, C. Poussard, M. Petit, Y. Monerie, C. Bernaudat, P. Yvon, X. Averty, The PROMETRA program: Fuel cladding mechanical behavior under high strain rate, *Nuclear Technology* 157 (3) (2007) 215–229. doi:10.13182/NT07-A3814.
- [18] H. Abe, T. Abe, S. Kishita, S. Kano, Y. Li, K. Tawara, Y. Matsukawa, Y. Satoh, Development of advanced expansion due to compression (A-EDC) test method for safety evaluation of degraded nuclear fuel cladding materials, *Journal of Nuclear Science and Technology* 52 (10) (2015) 1232–1239. doi:10.1080/00223131.2015.1056560.
- [19] A. Chaieb, N. Mozzani, A. Parrot, A. Ambard, Anisothermal behaviour of unirradiated CWSR zircaloy-4 fuel clads under RIA conditions, in: *TopFuel*, Prague, 2018.
- [20] J. Papin, B. Cazalis, J. M. Frizonnet, J. Desquines, F. Lemoine, V. Georgenthum, F. Lamare, M. Petit, Summary and Interpretation of the CABRI REP-Na Program, *Nuclear Technology* 157 (3) (2007) 230–250. doi:10.13182/NT07-A3815.
- [21] M. Ishikawa, S. Shiozawa, A study of fuel behavior under reactivity initiated accident conditions, *Journal of Nuclear Materials* 95 (1-2) (1980) 1–30. doi:10.1016/0022-3115(80)90076-8.
- [22] D. Campello, N. Tardif, M. Moula, M. C. Baietto, M. Coret, J. Desquines, Identification of the steady-state creep behavior of Zircaloy-4 claddings under simulated Loss-Of-Coolant Accident conditions based on a coupled experimental/numerical approach, *International Journal of Solids and Structures* 115-116 (2017) 190–199. doi:10.1016/j.ijsolstr.2017.03.016.
- [23] D. Campello, N. Tardif, J. Desquines, M. C. Baietto, M. Coret, A. Maynadier, P. Chaudet, Validation of a multimodal set-up for the study of zirconium alloys claddings’ behaviour under simulated LOCA conditions, *Strain* 54 (5) (2018) 1–14. doi:10.1111/str.12279.
- [24] T. Jailin, N. Tardif, J. Desquines, M. Coret, M. C. Baietto, T. Bréville, P. Chaudet, V. Georgenthum, Mechanical Behavior of As-Fabricated Zircaloy-4 Claddings Under the Simulated Thermo-Mechanical Post-DNB Conditions of a Reactivity Initiated Accident (RIA), in: *Top Fuel*, European Nuclear Society, Prague, 2018.
- [25] T. Jailin, N. Tardif, J. Desquines, M. Coret, T. Bréville, P. Chaudet, M. C. Baietto, V. Georgenthum, C. Bernaudat, Multimodal setups for the study of fresh Zircaloy-4 claddings under simulated thermal-mechanical RIA conditions, in: *PhotoMechanics*, Toulouse, 2018.
- [26] F. Li, T. Mihara, Y. Udagawa, M. Amaya, The effect of hydride morphology on the failure strain of stress-relieved Zircaloy-4 cladding with an outer surface pre-crack under biaxial stress states, *Journal of Nuclear Science and Technology* 56 (5) (2019) 432–439. doi:10.1080/00223131.2019.1592723.
- [27] N. Tardif, M. Coret, A. Combescure, Experimental study of the fracture kinetics of a tubular 16MnNiMo5 steel specimen under biaxial loading at 900 and 1000°C. Application to the rupture of a vessel bottom head during a core meltdown accident in a pressurized water reactor, *Nuclear Engineering and Design* 241 (3) (2011) 755–766. doi:10.1016/j.nucengdes.2011.01.026.
- [28] J. Réthoré, Muhibullah, T. Elguedj, M. Coret, P. Chaudet, A. Combescure, Robust identification of elasto-plastic constitutive law parameters from digital images using 3D kinematics, *International Journal of Solids and Structures* 50 (1) (2013) 73–85. doi:10.1016/j.ijsolstr.2012.09.002.
- [29] J. Réthoré, Ufreckles v2 (2018). doi:10.5281/zenodo.1433776.
- [30] T. Jailin, N. Tardif, J. Desquines, M. Coret, M. C. Baietto, T. Bréville, P. Chaudet, V. Georgenthum, Coupled NIRT / 3D-DIC for a FEMU identification of the thermo-mechanical behavior of Zr-4 claddings under simulated Reactivity Initiated Accident, in: *Proc. of SEM 2019 Annual Conference*, Reno, 2019.
- [31] T. Jailin, N. Tardif, J. Desquines, M. Coret, M. C. Baietto, V. Georgenthum, Experimental study and modelling of the phase transformation of Zircaloy-4 alloy under high thermal transients, In Press.
- [32] J. Qu, M. Cherkaoui, *Fundamentals of micromechanics of solids*, Wiley Hoboken, 2006. doi:10.1002/9780470117835.